

## Insertion of MXene-Based Materials into Cu–Pd 3D Aerogels for Electroreduction of CO<sub>2</sub> to Formate

Abdinejad, Maryam; Subramanian, Siddhartha; Motlagh, Mozghan Khorasani; Ripepi, Davide; Pinto, Donato; Li, Mengran; Middelkoop, Joost; Urakawa, Atsushi; Burdyny, Thomas; More Authors

**DOI**

[10.1002/aenm.202300402](https://doi.org/10.1002/aenm.202300402)

**Publication date**

2023

**Document Version**

Final published version

**Published in**

Advanced Energy Materials

**Citation (APA)**

Abdinejad, M., Subramanian, S., Motlagh, M. K., Ripepi, D., Pinto, D., Li, M., Middelkoop, J., Urakawa, A., Burdyny, T., & More Authors (2023). Insertion of MXene-Based Materials into Cu–Pd 3D Aerogels for Electroreduction of CO<sub>2</sub> to Formate. *Advanced Energy Materials*, 13(19), Article 2300402. <https://doi.org/10.1002/aenm.202300402>

**Important note**

To cite this publication, please use the final published version (if applicable). Please check the document version above.

**Copyright**

Other than for strictly personal use, it is not permitted to download, forward or distribute the text or part of it, without the consent of the author(s) and/or copyright holder(s), unless the work is under an open content license such as Creative Commons.

**Takedown policy**

Please contact us and provide details if you believe this document breaches copyrights. We will remove access to the work immediately and investigate your claim.

***Green Open Access added to TU Delft Institutional Repository***

***'You share, we take care!' - Taverne project***

**<https://www.openaccess.nl/en/you-share-we-take-care>**

Otherwise as indicated in the copyright section: the publisher is the copyright holder of this work and the author uses the Dutch legislation to make this work public.

# Insertion of MXene-Based Materials into Cu–Pd 3D Aerogels for Electroreduction of CO<sub>2</sub> to Formate

Maryam Abdinejad,\* Siddhartha Subramanian, Mozghan Khorasani Motlagh, Meissam Noroozifar, Salatan Duangdangchote, Ihor Neporozhnii, Davide Ripepi, Donato Pinto, Mengran Li, Keith Tang, Joost Middelkoop, Atsushi Urakawa, Oleksandr Voznyy,\* Heinz-Bernhard Kraatz,\* and Thomas Burdyny\*


The electrochemical CO<sub>2</sub> reduction reaction (CO<sub>2</sub>RR) is an attractive method to produce renewable fuel and chemical feedstock using clean energy sources. Formate production represents one of the most economical target products from CO<sub>2</sub>RR but is primarily produced using post-transition metal catalysts that require comparatively high overpotentials. Here a composition of bimetallic Cu–Pd is formulated on 2D Ti<sub>3</sub>C<sub>2</sub>T<sub>x</sub> (MXene) nanosheets that are lyophilized into a highly porous 3D aerogel, resulting in formate production much more efficient than post-transition metals. Using a membrane electrode assembly (MEA), formate selectivities >90% are achieved with a current density of 150 mA cm<sup>-2</sup> resulting in the highest ever reported overall energy efficiency of 47% (cell potentials of –2.8 V), over 5 h of operation. A comparable Cu–Pd aerogel achieves near-unity CO production without the MXene templating. This simple strategy represents an important step toward the experimental demonstration of 3D-MXenes-based electrocatalysts for CO<sub>2</sub>RR application and opens a new platform for the fabrication of macroscale aerogel MXene-based electrocatalysts.

## 1. Introduction

As climate change concerns increase, serious efforts are required to mitigate the harmful emission of carbon dioxide

M. Abdinejad, S. Subramanian, D. Ripepi, D. Pinto, M. Li, J. Middelkoop, A. Urakawa, T. Burdyny  
Department of Chemical Engineering  
Delft University of Technology  
Van der Maasweg 9, Delft 2629 HZ, The Netherlands  
E-mail: maryamab@mit.edu; t.e.burdyny@tudelft.nl

M. K. Motlagh, M. Noroozifar, S. Duangdangchote, I. Neporozhnii, K. Tang, O. Voznyy, H.-B. Kraatz  
Department of Physical and Environmental Sciences  
University of Toronto Scarborough  
1265 Military Trail, Toronto, ON M1C 1A4, Canada  
E-mail: o.voznyy@utoronto.ca; bernie.kraatz@utoronto.ca

 The ORCID identification number(s) for the author(s) of this article can be found under <https://doi.org/10.1002/aenm.202300402>.

© 2023 The Authors. Advanced Energy Materials published by Wiley-VCH GmbH. This is an open access article under the terms of the Creative Commons Attribution License, which permits use, distribution and reproduction in any medium, provided the original work is properly cited.

DOI: 10.1002/aenm.202300402

(CO<sub>2</sub>).<sup>[1]</sup> One of the most promising approaches is converting CO<sub>2</sub> to value-added materials through an electrochemical CO<sub>2</sub> reduction reaction (CO<sub>2</sub>RR) using renewable electricity.<sup>[2,3]</sup> Despite the potential of CO<sub>2</sub>RR technology, there are still significant challenges in both fundamental (e.g., catalyst activity, selectivity, and durability) and system aspects (e.g., mass transport, conversion rate, and energy efficiency), which need to be addressed.<sup>[4,5]</sup> In aqueous environments, CO<sub>2</sub>RR can produce a number of reduced materials, including C1 products, such as CO and formate, and C<sub>2</sub> products, like acetate, ethylene, and ethanol.<sup>[6–10]</sup> Formate, in particular, represents the most economically-viable reduction product from CO<sub>2</sub> due to its industrial value and requirement of only 2 electrons.<sup>[11,12]</sup>

To date, the majority of catalysts able to produce formate through CO<sub>2</sub>RR are pure post-transition metal catalysts such as Sn,<sup>[9,13–16]</sup> In,<sup>[17,18]</sup> and Pb,<sup>[19,20]</sup>; however, large overpotentials are required to activate CO<sub>2</sub> on these metals compared to transition metal catalysts for CO production. Therefore, further catalyst design is necessary to optimize CO<sub>2</sub>-to-formate conversion and improve energy efficiency at high current densities (>150 mA cm<sup>-2</sup>) suitable for potential industrial applications. Researchers have found success using a number of bimetallic post-transition metal containing catalysts, where the catalyst interface is engineered to contain more active sites and to tune intermediate binding energies. For example, recently, Ren et al.,<sup>[21]</sup> reported high FE<sub>formate</sub> (>90%) with a current density of ≈140 mA cm<sup>-2</sup> using a Sn–Bi catalyst, highlighting the importance of bimetallic catalytic engineering design to improve the overall catalytic performance.

Separately, transition metals such as Ag and Cu catalysts can also activate CO<sub>2</sub> to formate, although as a minor product. Copper-based electrocatalysts in particular are commonly employed in the CO<sub>2</sub>RR process to produce a range of products including CO, formate and hydrocarbons.<sup>[22,23]</sup> One approach for formate production has been to pair Cu catalysts with other metals. The binding strength of Cu alone catalyst to a CO<sub>2</sub> may have a regulatory effect, where intermediate binding may not

sufficiently activate the molecule, while those that bind too strongly become poisoned.<sup>[24]</sup> For example, Sn-Cu alloys have shown high selectivity toward formate and CO production that are more efficient than Sn alone.<sup>[14,25]</sup> Notably, when paired with Sn, the production of ethylene and ethanol are greatly decreased, indicating that further reduction of CO is restricted. Similarly, alloying Cu to Pd has been an approach to significantly enhance the production of CO and formate<sup>[26–30]</sup> owing to the strong H affinity with Pd surface,<sup>[30,31]</sup> which increases the potential barrier of CO\* protonation step,<sup>[26,27]</sup> as well as suppressing the activity of HERs.<sup>[24,32]</sup> Lower cell potentials and the presence of Cu further seem to prevent Pd poisoning by CO.

In addition to the choice of metal for the catalyst, morphology and a catalyst's support is another critical component in tuning catalytic performance and increasing extrinsic activity.<sup>[20]</sup> By increasing active area, lower potentials can be applied, which is not only critical for energy efficiency, but preventing cathode degradation and poisoning. MXenes are a relatively new family of 2D layered transition metal carbides/nitrides material with the chemical formula of  $M_{n+1}X_nT_x$ , where M = transition metals, X = C or N, and  $T_x$  = surface groups (such as =O, –OH, –F, etc.).<sup>[33]</sup> Their unique 2D structure and hexagonal lattice symmetry provide them with a high specific surface area, excellent electrical conductivity,<sup>[34–36]</sup> and unique mechanical stabilities.<sup>[37,38]</sup> These properties make them useful for various applications, including energy conversion and storage.<sup>[39–41]</sup> However, due to strong van der Waals forces between their stacked layers, they often suffer from aggregation, resulting in the loss of accessible surface area and active sites. Several approaches have proven successful in alleviating this issue, such as heteroatom doping, surface modification, and the use of interlayer spacers<sup>[42]</sup> and cross-linkers.<sup>[43]</sup> For instance, Yorulmaz et al.<sup>[38]</sup> observed a reduction in MXene interlayer restacking after incorporating transition metals while also seeing an increase in electron transfer and CO<sub>2</sub> adsorption.

Given the importance of surface morphology, porosity, and the number of active sites available for CO<sub>2</sub> conversion,<sup>[44]</sup> we aimed to pair 2D MXene ( $Ti_3C_2T_x$ ) with bimetallic Cu-Pd to form 3D Cu-Pd/MXene aerogels under a lyophilization process. The optimized Cu-Pd/MXene catalyst exhibits a maximum  $FE_{\text{formate}}$  of 79% at a low potential of –0.5 V versus RHE in an H-cell electrolyzer; which is 300 mV lower than the potential of a comparable Cu-Pd aerogel without MXene templating. When integrated into a zero-gap membrane electrode assembly (MEA), the Cu-Pd/MXene catalyst reached higher formate Faradaic efficiencies of 93% and a current density of 150 mA cm<sup>–2</sup> while reaching a full cell energy efficiency (EE) of 47%. To get insight into the reaction mechanism pathways and the role of MXene in surface adsorption and altering the intermediate binding energy, density functional theory (DFT) was conducted.

## 2. Results

### 2.1. Synthesis and Characterization

The Cu–Pd hydrogel was synthesized through a one-pot hydrothermal treatment reaction process (details in the Experimental

Section). The 2D MXene was synthesized using ammonium bifluoride (NH<sub>4</sub>HF<sub>2</sub>) for etching off the Al from Ti<sub>3</sub>AlC<sub>2</sub> (Figure S1, Supporting Information). The preprepared MXene was incorporated into the Cu-Pd,<sup>[45]</sup> to form Cu-Pd/MXene hydrogel, which not only reduces the MXene's layer tendency to restack but also increases the catalytic surface area available for CO<sub>2</sub>RR.<sup>[46,47]</sup> To convert the achieved hydrogel to an aerogel, lyophilization was applied to form a highly porous Cu-Pd/MXene hybrid aerogel with a 3D structure (Figure 1a).

The morphology of the synthesized aerogels was examined using Scanning Electron Microscopy (SEM). Figures S2 and S3 (Supporting Information) show the SEM images of bulk Ti<sub>3</sub>AlC<sub>2</sub> and exfoliated Ti<sub>3</sub>C<sub>2</sub>T<sub>x</sub>, which displayed a typical multilayer, accordion-like structure of stacked MXene sheets resembling exfoliated graphite.<sup>[48]</sup> This phenomenon was further confirmed by Energy Dispersive X-Ray spectroscopy (EDX). The elemental mapping shows a uniform distribution of C, O, Ti, Cu, and Pd, which further confirms the formation of the successful synthesis of the catalysts (Figures S4–S6, Supporting Information). The removal of Al is also observed, while the presence of F and O indicates possible surface termination in the exfoliated process (Figures S7–S9, Supporting Information). The different morphology of the porous Cu-Pd aerogel (Figure 1b; Figure S10, Supporting Information) compared to the nanosheet-layered structure of Cu-Pd/MXene (Figure 1c; Figure S12, Supporting Information) was observed. The SEM of the Cu–Pd/MXene sample displayed MXene nanosheets acting as the main skeleton, which contained Cu–Pd distributed on the surface and within the layers forming Cu–Pd/MXene composite (Figure 1c; Figures S13–S15, Supporting Information).

The compositional and structural analyses of the synthesized catalysts were characterized by powder X-ray diffraction (XRD) and X-ray photoelectron spectroscopy (XPS) to confirm the catalysts' synthesis. The XRD measurements were conducted to determine the crystal structure of the materials before and after NH<sub>4</sub>HF<sub>2</sub>/HCl etching. Figure S16 (Supporting Information) shows the XRD patterns comparison of Ti<sub>3</sub>AlC<sub>2</sub> and Ti<sub>3</sub>C<sub>2</sub>T<sub>x</sub>. The observed typical peaks of both Ti<sub>3</sub>AlC<sub>2</sub> and Ti<sub>3</sub>C<sub>2</sub>T<sub>x</sub> samples were in agreement with the previously reported results.<sup>[49]</sup> Furthermore, the Pd-Cu and Pd-Cu/MXene compositions were confirmed by their XRD pattern shown in Figure 1d and Figure S17 (Supporting Information). The peaks corresponding to crystalline Cu (ca. 43.3°, 50.4°, 74.1°, and 89.9°) are not identified or negligible. Four peaks at 2θ values of 40.2°, 47.8°, 68.2°, and 82.2° are characteristic of crystalline Pd assigned to the planes (111), (200), (220), and (311), respectively. Higher 2θ angles were observed in the case of Cu–Pd and Cu–Pd/MXene compared to monometallic Pd and Cu, which reflects the interaction of Pd and Cu atoms suggesting the successful formation of the bimetallic Cu–Pd. The results are in agreement with previous reports.<sup>[50–52]</sup>

The XPS survey comparison of Cu–Pd and Cu–Pd/MXenes further confirmed the presence of Pd, Cu, and Ti elements with the absence of Ti peak at Cu–Pd (Figure 1e). The peaks at 457.28 and 462.83 eV correspond to Ti 2p<sub>1/2</sub> and Ti 2p<sub>3/2</sub> (Figure S18, Supporting Information). The Pd 3d<sub>5/2</sub> core-level binding energy of Cu–Pd and Cu–Pd/MXene was observed at 335.48 and 335.28 eV, respectively (Figure 1f; Figures S19a and S20a, Supporting Information). This slight shift could be associated

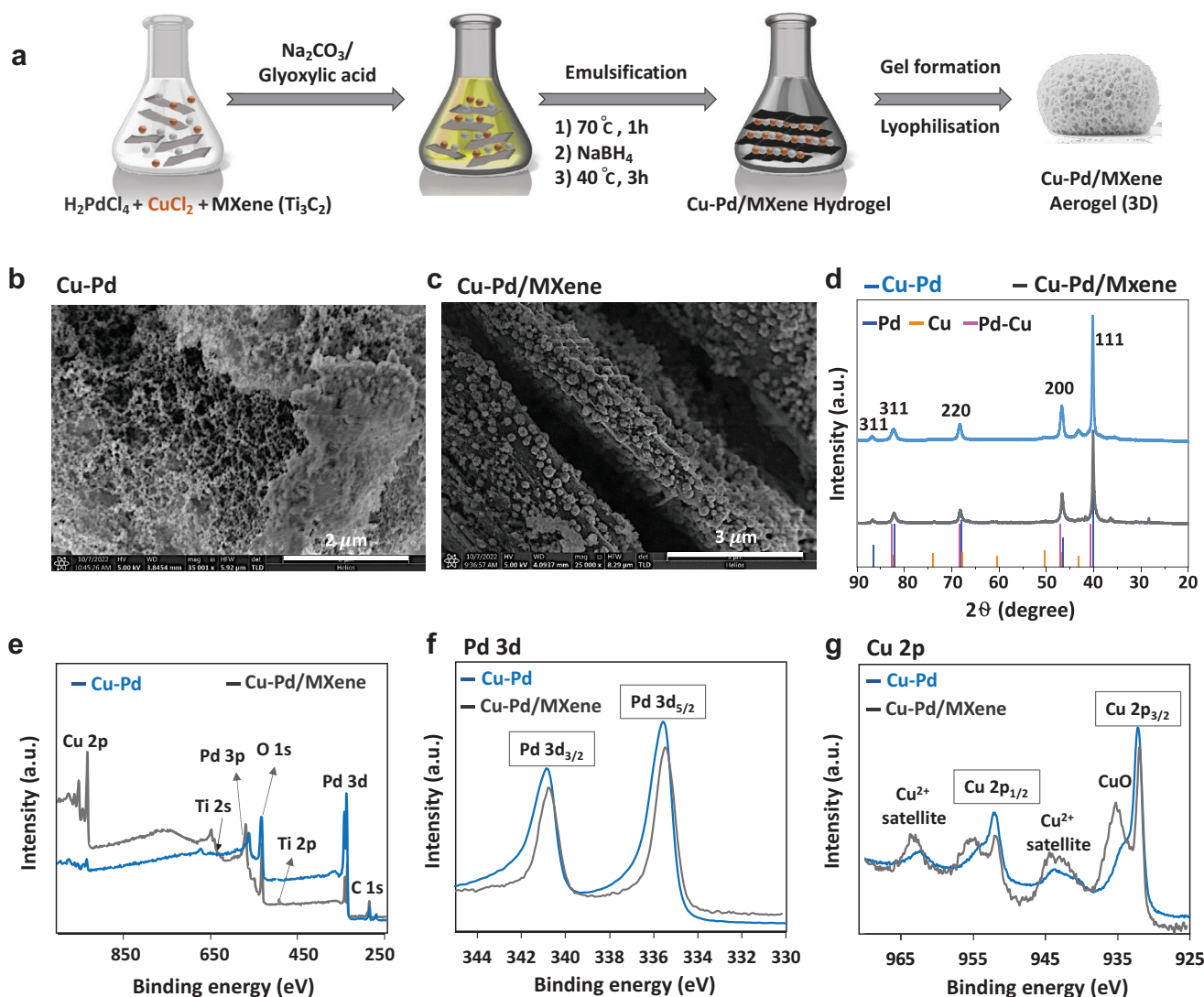


**Figure 1.** Preparation and characterization of Cu/Pd MXene material. a) Schematic of Cu-Pd/MXene preparation. Scanning electron microscopy (SEM) of b) Cu-Pd; and c) Cu-Pd/MXene. d) X-ray diffraction analysis (XRD) comparison of Cu-Pd and Cu-Pd/MXene. e) X-ray photoelectron spectroscopy (XPS) survey spectra of Cu-Pd and Cu-Pd/MXene. The XPS comparison of f) Pd 3d; and g) Cu 2p spectra of Cu-Pd and Cu-Pd/MXene.

with Cu-Pd and Ti interactions in the Cu-Pd/MXene composition.<sup>[53,54]</sup> The characteristic Cu 2p<sub>1/2</sub> and Cu 2p<sub>3/2</sub> peaks at 951.8 and 932.1 eV are ascribed to Cu(I),<sup>[55]</sup> and the weaker peaks at 935.1 and 943.6 eV belong to Cu(II) (Figure 1g; Figures S19b and S20b, Supporting Information).<sup>[56]</sup> With characterization complete, the catalysts were tested for reactivity toward electrochemical CO<sub>2</sub>RR.

## 2.2. Electrochemical CO<sub>2</sub> Reduction in an H-cell

The catalytic activity of Cu-Pd and Cu-Pd/MXene catalysts were tested for CO<sub>2</sub> electroreduction in a gas-tight two-compartment H-cell in 0.1 M KHCO<sub>3</sub> aqueous solution as catholyte and anolyte.<sup>[7]</sup> To prepare the working electrode, the mixture of each synthesized catalyst (5 mg) in DMF (2 mL) with Nafion (2%) was sonicated for 10 min to obtain a well-mixed suspension.

Next, 5 μL of the resulting suspension was drop-casted on the pre-prepared 0.3 cm diameter glassy carbon surface electrode and left to dry for 24 h.

To determine the catalytic activity of the synthesized catalysts toward CO<sub>2</sub>, linear sweep voltammogram (LSV) comparison of bare MXene, Cu-Pd, Cu-Pd/MXene was performed at 0.1 M KHCO<sub>3</sub> aqueous solution under both Ar and CO<sub>2</sub> for a systematic comparison (Figure S21, Supporting Information). As shown in Figure 2a, exposure of the catalysts to CO<sub>2</sub> resulted in higher current density and a shift to a more positive potential in the case of Cu-Pd/MXene. Based on the observed onset potentials in Figure 2a, we then performed chronoamperometry at constant applied potentials of -0.2 to -0.9 V versus RHE to determine the formed electrochemical products and their selectivity (Figure S22, Supporting Information). Gas products were detected by gas chromatograph (GC), while liquid products were identified and analyzed with high-performance liquid



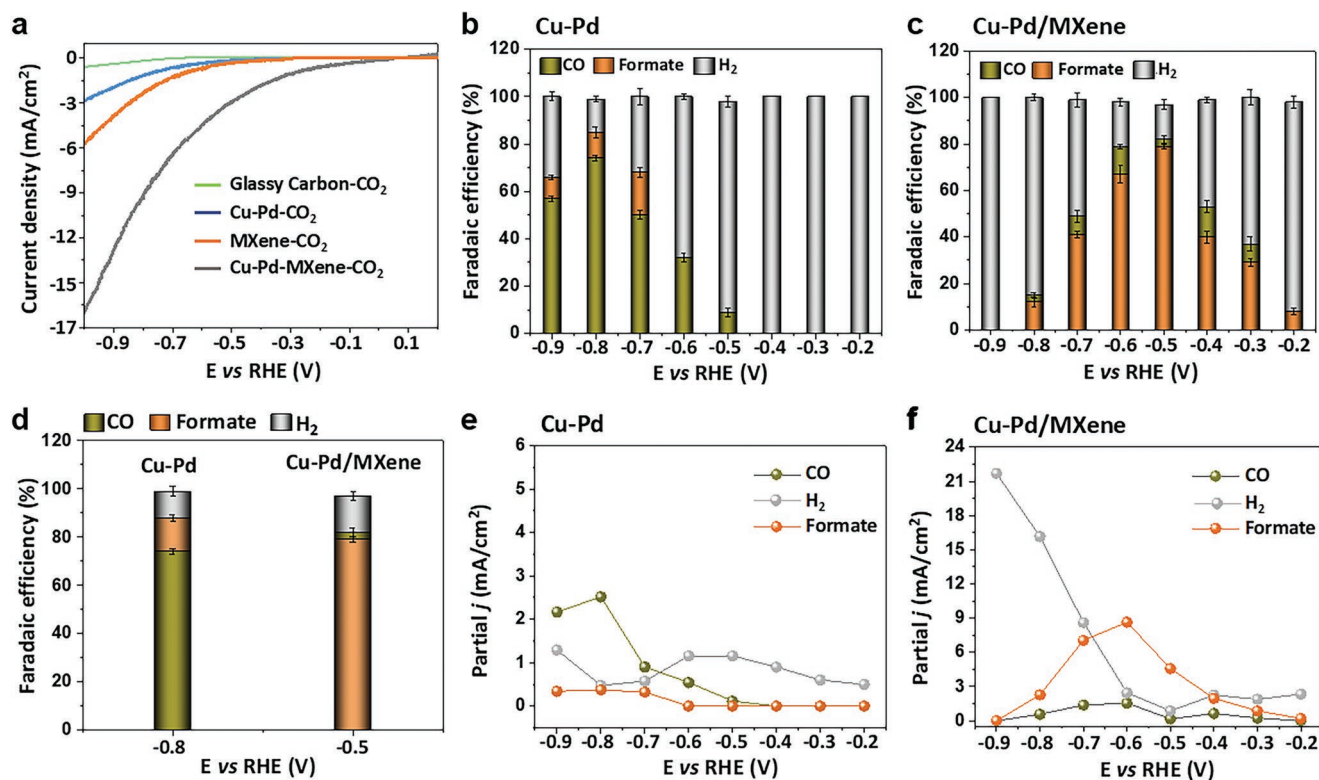


**Figure 2.** Results of electroreduction of CO<sub>2</sub> in H-cell environment. a) Linear sweep voltammetry (LSV) comparison of glassy carbon electrode, Cu-Pd, and Cu-Pd/MXene under CO<sub>2</sub> in 0.1 M KHCO<sub>3</sub>. Faradaic efficiency (FE) comparison of b) Cu-Pd; and c) Cu-Pd/MXene at -0.2 to -0.9 V versus RHE in 0.1 M KHCO<sub>3</sub>. d) FE comparison of Cu-Pd and Cu-Pd/MXene at the optimal potential of -0.8 and -0.5 V versus RHE, respectively. Partial current density comparison of e) Cu-Pd; and f) Cu-Pd/MXene at -0.2 to -0.9 V versus RHE in 0.1 M KHCO<sub>3</sub>.

chromatography (HPLC) and proton nuclear magnetic resonance (<sup>1</sup>H NMR) (Figures S23 and S24, Supporting Information).

In the case of Cu-Pd, CO was achieved as the main reduced product with a maximum selectivity of 74% at -0.8 V versus RHE (Figure 2b). Applying the same potentials for Cu-Pd/MXene electrocatalyst, formate was observed as a major product of CO<sub>2</sub>RR with the highest selectivity of 79% at a potential of -0.5 V versus RHE (Figure 2c). We observed a decrease in the formate FE at higher potentials, which could be due to increasing HER at more negative potentials. When comparing the peak CO<sub>2</sub> reduction performance of the Cu-Pd and Cu-Pd/MXene samples, we see three distinct differences. First, the onset potential for the MXene sample was 300 mV lower than the Cu-Pd aerogel (Figure 2d). Second, we see different C1 product FE's, although notably the peak partial current density for CO has a similar trend for both samples (Figure 2e,f). And lastly, the exhibited current densities for Cu-Pd/MXene sample are substantially higher, which could be due MXene's greater surface area and higher access to CO<sub>2</sub>. It should be noted that employing the bare MXene under the same conditions, H<sub>2</sub> was observed as a sole product and no CO<sub>2</sub> reduced products were observed, indicating the importance of the Cu and Pd sites for CO<sub>2</sub>RR.

The comparison of the product partial current densities for Cu-Pd and Cu-Pd/MXene in Figure 2e,f shows similar amounts of CO, but with Cu-Pd/MXene produces substantially more formate. The formate partial current density started

decreasing at a more negative potential than -0.5 V versus RHE. This can be attributed to the mass transport limitation of the reactant on the catalyst surface in the H-cell configuration as well as the competitive H<sub>2</sub> evolution reaction at a higher potential.<sup>[13]</sup> Further, in the H-cell configuration, a substantial surface area of the MXene catalyst likely does not have CO<sub>2</sub> access, and is then left only available for hydrogen production in CO<sub>2</sub> depleted regions.<sup>[57]</sup> For these reasons full assessment of the catalyst needs to be done in a CO<sub>2</sub>-rich testing platform such as a zero-gap membrane electrode assembly.

### 2.3. Electrochemical CO<sub>2</sub> reduction in MEA cell

To improve the mass transport, current density and overall catalytic performance, a MEA cell containing an anode chamber with a liquid phase anolyte (0.5 M KOH) and a cathode chamber with a gas phase inlet were assessed (Figure 3a; Figures S25-S27, Supporting Information).<sup>[58]</sup> The gas diffusion electrodes (GDE) were prepared by depositing the synthesized catalysts onto the base gas diffusion layers (GDL) (details in the Experimental Section). The MEA cell design can achieve much higher current densities than H-cells because gaseous CO<sub>2</sub> is delivered in close proximity to a liquid-immersed catalyst. The substantially higher surface area provided by a 3D catalyst layer with full access to CO<sub>2</sub> then also allows for lower cell potentials as the entirety of the catalytic area can be active.<sup>[59]</sup>

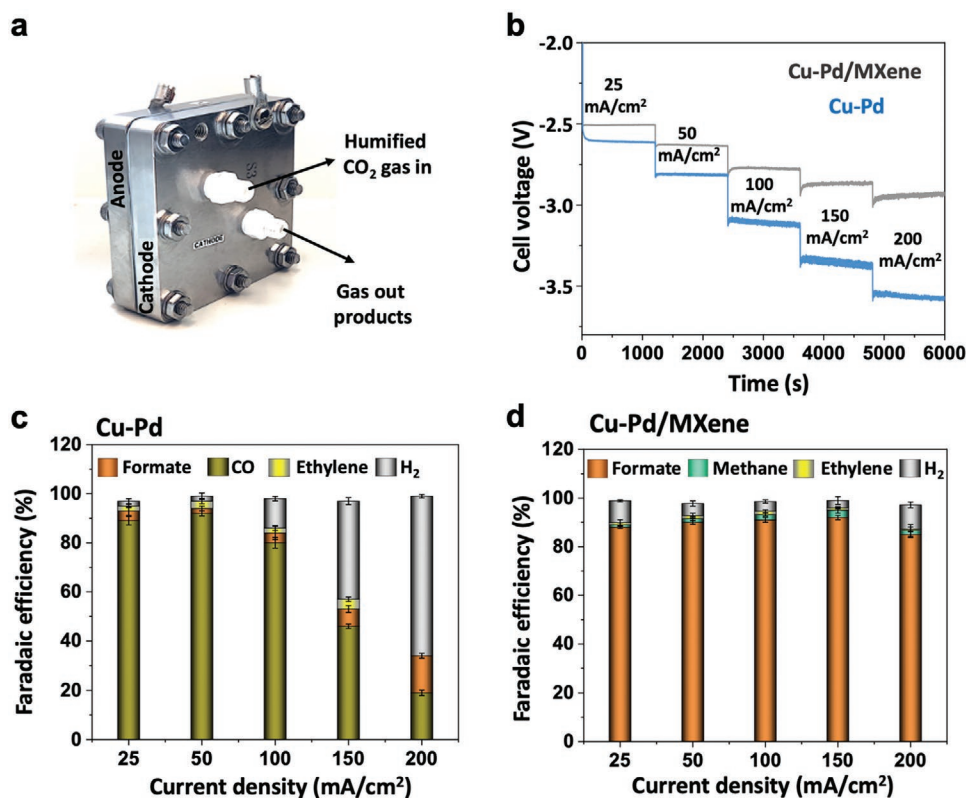


**Figure 3.** Results of electroreduction of  $\text{CO}_2$  using membrane electrode assembly (MEA). a) MEA cell for the electrochemical reduction of  $\text{CO}_2$ ; b) Sketch graph of voltage against time at different current steps in the range of 25, 50, 100, 150, and 200  $\text{mA cm}^{-2}$ ; Faradaic efficiency (FE) comparison of c) Cu–Pd; and d) Cu–Pd/MXene at current densities of 25, 50, 100, 150, and 200  $\text{mA cm}^{-2}$  in 0.5 M KOH using MEA cell.

To study the cell potential of the catalysts in the MEA cell, stepwise constant current densities of 25–200  $\text{mA cm}^{-2}$  were applied, as shown in Figure 3b. The cell voltage was measured and increased with increasing current density. Here the Cu–Pd/MXene catalyst demonstrated cell potentials of 300–400 mV lower than the Cu–Pd aerogels at equivalent current densities. In this configuration, each catalyst benefits from higher surface areas than the H-cell test, but the MXene catalyst still appears to benefit from greater surface sites.

During these chronopotentiometry scans, product selectivity was also measured. The gas products were collected from the cathode and characterized with GC, while the liquid products were collected from anolyte and characterized with both  $^1\text{H}$  NMR and HPLC. Using Cu–Pd, the primary observed product was again CO, reaching 91% at 50  $\text{mA cm}^{-2}$  (Figure 3c; and Table S2, Supporting Information). At elevated current densities, the partial current density of CO then peaked at 80  $\text{mA cm}^{-2}$  before declining at higher overall reaction rates. This could indicate lower stability of the Cu–Pd aerogel leading to reduced  $\text{CO}_2\text{RR}$  current densities and a resulting increase in HER. In the case of Cu–Pd/MXene, formate was observed as the primary product at all current densities, similar to the H-cell experiments (Figure 3d), with the highest catalytic activity at 150  $\text{mA cm}^{-2}$ . Here the  $\text{FE}_{\text{formate}}$  was measured as 93% at a cell voltage of  $-2.8$  V, leading to an average EE of 47% for formate. In addition, trace amounts of methane and ethylene (indicative of C–C coupling) were also detected. Comparing partial current

densities of  $\text{H}_2$  in Figure S28 (Supporting Information), as the current increases,  $\text{H}_2$  begins to increase, and HER becomes a dominant reaction, especially at the higher current density of 150 and 200  $\text{mA cm}^{-2}$ .<sup>[59,60]</sup>

To gain insight into the importance of synergy between MXene surface and Cu–Pd catalysts, a control experiment was performed with a physical mixture of MXene and Cu–Pd (1:1 ratio). The mixture was deposited onto GDE, and the stepwise constant current densities of 25–200  $\text{mA cm}^{-2}$  were conducted. The results were also compared with the bare MXene for systematic comparison (Figure S29 and Table S2, Supporting Information). For the mixed Cu–Pd+MXene case, with increasing current density, the FE of formate decreased while CO increased (Figure S30, Supporting Information). The FE of  $\text{H}_2$  increased to 69% at the current density of 200  $\text{mA cm}^{-2}$ . The result highlights the combined importance of the Cu and Pd intercalation of the MXene layers, and the catalytic availability of Cu–Pd when on a MXene support instead of in a pure aerogel form.

Additional materials and electrochemical characterizations were applied to get more information about the synthesized catalysts' properties. First,  $\text{CO}_2$  adsorption capacity measurements were conducted using thermogravimetric analysis (TGA) (Figure 4a; Figure S31, Supporting Information).<sup>[61,62]</sup> The samples (ca. 10 mg) were placed into the TGA measuring pan, and the temperature was increased from 25 to 80  $^\circ\text{C}$  at a heating rate of 10  $^\circ\text{C min}^{-1}$  and equilibrated at 80  $^\circ\text{C}$  for 1 h

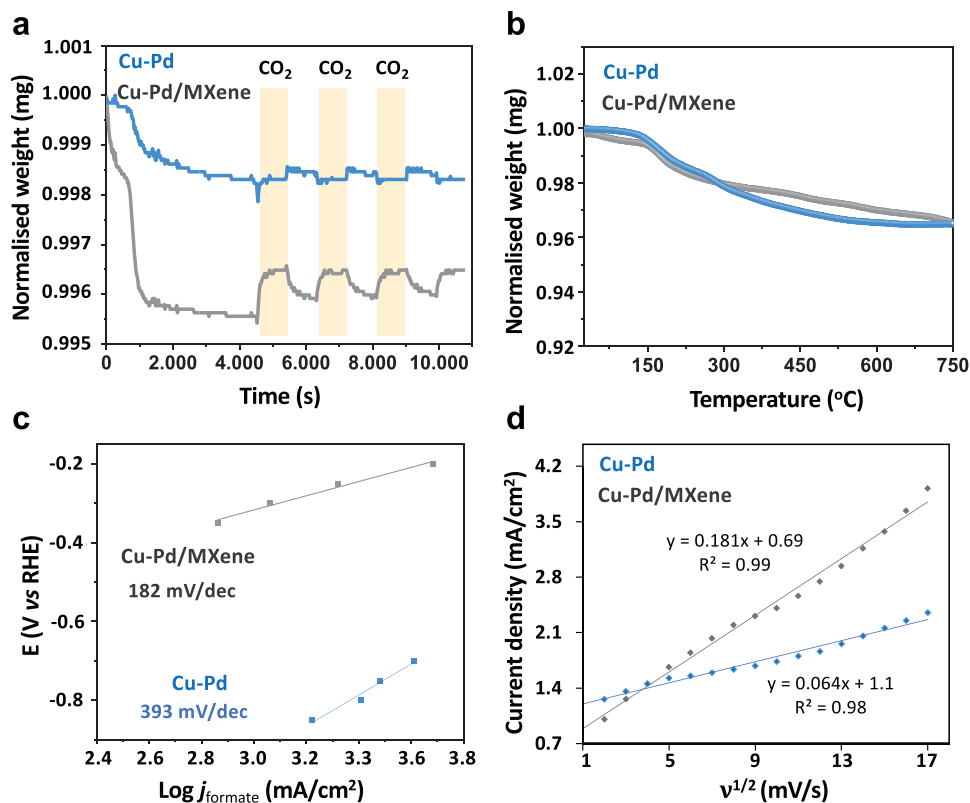


**Figure 4.** a) The CO<sub>2</sub> adsorption capacity of Cu-Pd and Cu-Pd/MXene was measured by thermogravimetric analysis (TGA) at 80 °C. b) Stability test of Cu-Pd and Cu-Pd/MXene at the temperature range of 25 to 750 °C using TGA. c) Tafel slopes for the current density of Cu-Pd and Cu-Pd/MXene at -0.2, -0.3, -0.4, and -0.5 V versus RHE in 0.1 M KHCO<sub>3</sub> using H-cell. d) The plot of forward peak current density versus the square root of Cu-Pd and Cu-Pd/MXene with the scan rates of 10–140 mV s<sup>-1</sup>.

under N<sub>2</sub> with a flow rate of 100 mL min<sup>-1</sup>. Next, the sample was cyclically exposed to CO<sub>2</sub> and N<sub>2</sub> pulses at the same temperature. The weight change of the sample measured by TGA during adsorption/desorption processes determined the CO<sub>2</sub> adsorption capacity of the samples. A higher CO<sub>2</sub> adsorption was clearly observed using Cu-Pd/MXene, and negligible in the case of Cu-Pd. For the Cu-Pd/MXene sample, a CO<sub>2</sub> adsorption of 0.9 mg g<sub>cat</sub><sup>-1</sup> has been detected, corresponding to 0.02 mmol g<sup>-1</sup>. Such a value is only one order of magnitude lower than typical CO<sub>2</sub> solid sorbents.<sup>[63,64]</sup> Next, the thermal stability of the synthesized catalysts was examined by heating the samples from 25 to 750 °C under N<sub>2</sub> with 10 °C min<sup>-1</sup> heating rate (Figure 4b). High thermal stability with a slight weight loss was observed in this high-temperature range which makes Cu-Pd/MXene a promising catalyst to be conducted in electrocatalytic CO<sub>2</sub> and other applications.

We further attribute the higher CO<sub>2</sub>RR performance of Cu-Pd/MXene to a larger surface area and higher electron transfer, as confirmed by Tafel and capacitance-based electrochemical surface area (ECSA) measurements. It is known that a two electron-transfer process is involved in the electroreduction of CO<sub>2</sub> to CO and formate. Cu-Pd/MXene and Cu-Pd exhibited a Tafel slope of 182 and 393 mV dec<sup>-1</sup> (Figure 4c), respectively, which shows that the first electron transfer for CO<sub>2</sub> activation is the rate-determining step (RDS) for the overall process.<sup>[65,66]</sup> Observing a lower Tafel slope in the case of Cu-Pd/MXene, suggests that Cu-Pd/MXene has a more rapid initial electron

transfer step for the CO<sub>2</sub><sup>-</sup> formation, which improves the formate generation.<sup>[67–69]</sup>

Next, ECSA was calculated using the rate of electron transfer between the solid support and catalysts with cyclic voltammetry (CV) at several scan rates of 10–140 mV s<sup>-1</sup> (Figure 4d; Figure S32, Supporting Information).<sup>[70]</sup> A linear relationship between the reduction peak currents and the square root of the scan rate (v<sup>1/2</sup>) in Figure 4d confirms the larger active surface area and electron transfer rate belonging to Cu-Pd/MXene (0.181 cm<sup>2</sup>) compared to Cu-Pd (0.064 cm<sup>2</sup>). This can be attributed to the improvement in electron transfer and a larger electrochemically active surface area provided by the MXene solid support. A larger ECSA could provide larger catalytically active sites,<sup>[71]</sup> and facilitate the CO<sub>2</sub>RR intermediates adsorptivity on the catalyst's surface,<sup>[72]</sup> which might be the reason for observing better catalytic performance for Cu-Pd/MXene.

We further demonstrate the stability of Cu-Pd/MXene at over 5 h electrolysis at the optimal current density of 150 mA cm<sup>-2</sup>. As shown in Figure 5a, the Cu-Pd/MXene catalysts stayed stable at the constant current density of 150 mA cm<sup>-2</sup> and cell voltage of -2.8 V over the test. After the 5 h electrolysis, the FE<sub>formate</sub> was still ~90%, with an average EE of 47% (Figure 5b). Based on the SEM shown in Figure S33 (Supporting Information), Cu-Pd/MXene could maintain its layered structure after long-term stability testing. Running the reaction for more than 5 h (Figure S34, Supporting Information) resulted in an increase in cell potential and loss of selectivity due to salt precipitation which blocks the CO<sub>2</sub>



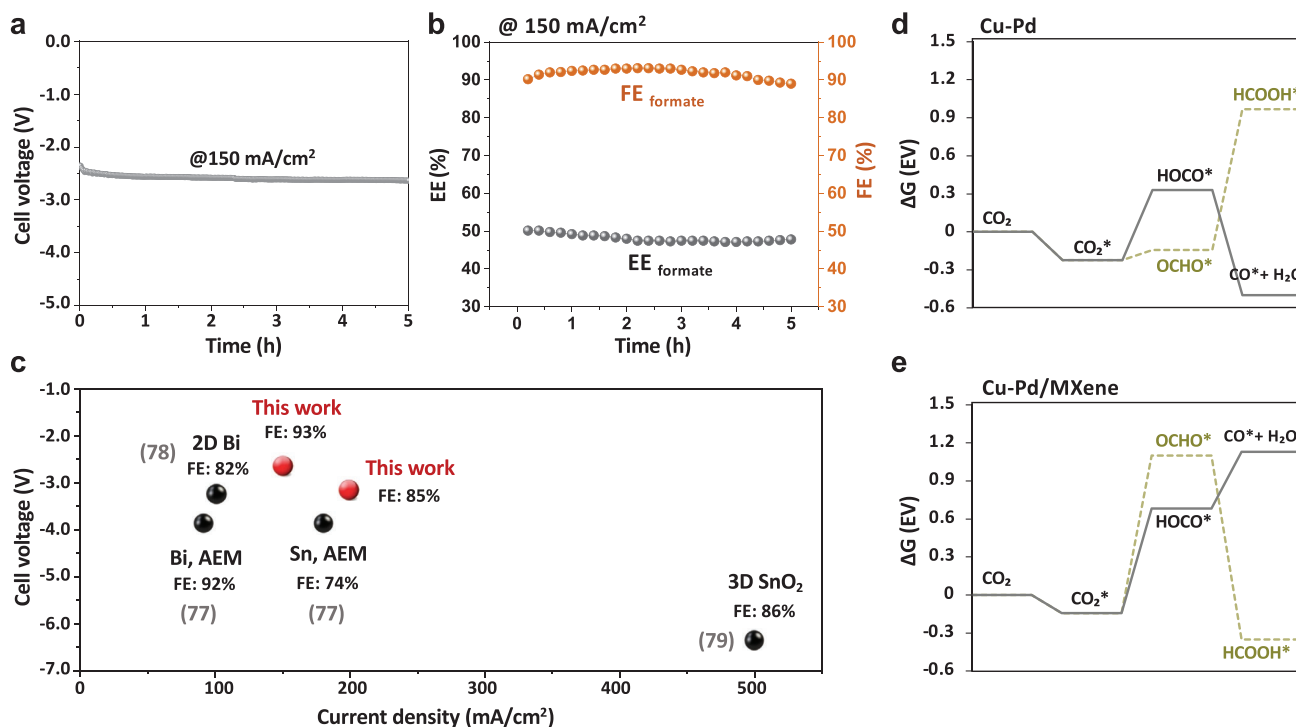


**Figure 5.** The catalytic stability performance. a) long-term stability studies of Cu–Pd/MXene for CO<sub>2</sub> electroreduction operated at 150 mA cm<sup>-2</sup> for 5 h in 0.5 M KOH using MEA cell. b) The Faradaic efficiency (FE) of CO<sub>2</sub> electroreduction to formate and energy conversion efficiency (EE) of CO<sub>2</sub> to formate over 5 h in 0.5 M KOH at an applied current density of 150 mA cm<sup>-2</sup>. c) Comparison of our work with previously published literature benchmarks. CO<sub>2</sub>RR pathway plot for d) Cu–Pd, and e) Cu–Pd/MXene using Density Functional Theory (DFT).

transport to the active catalytic sites in the cathode (Figure S35, Supporting Information).<sup>[73]</sup> Currently, various strategies such as pulsed operation,<sup>[74]</sup> periodic water flushing<sup>[75]</sup> and the use of dilute anolyte concentrations delay salt precipitation; however, each strategy comes with a trade-off in compromising on a higher cell voltage or flooding of GDE over time.<sup>[76]</sup>

Figure 5c, and Table S4 (Supporting Information) confirm that Cu–Pd/MXene performs the lowest cell potential with the highest formate selectivity among the highest reported in the literature using MEA cell.<sup>[77–79]</sup>

### 3. Discussion

As demonstrated in this project, the bimetallic Cu–Pd electrocatalyst was able to promote CO production, consistent with previous reports using Cu–Pd-based catalysts.<sup>[26,27]</sup> By switching Cu–Pd with Cu–Pd/MXene the overall catalytic performance was improved and C1 product formation was shifted from CO to formate. This dramatic change to the catalytic selectivity of Cu–Pd and Cu–Pd/MXene could be related to the difference in the catalysts' surface adsorption properties and their energy barrier toward CO<sub>2</sub>RR intermediates.<sup>[80,81]</sup> This task was examined with DFT calculation (Figure S36, Supporting Information). In the absence of atomically-resolved Cu–Pd/MXene surface, the hypothetical structure of MXene with Pd adatom was used to assess the energetics of Cu–Pd/MXene. The two possible reduction pathways from CO<sub>2</sub> to HCOOH (formate route) and CO<sub>2</sub> to CO (CO route) in Figure 5d,e indicate that the CO<sub>2</sub> adsorption

on Cu–Pd (–0.189 eV) is stronger than on Cu–Pd/MXene with adsorption energies of –0.109. The formation of CO\* seems to be more thermodynamically favorable in both Cu–Pd and Cu–Pd/MXene cases. However, MXene substrate did cause a significant change in the energy barriers of the reaction.

In summary, we observed a suppression of CO production in favor of highly selective formate production with high activity and stability. Despite this, only a few studies report MXenes as solid supports for aerogel catalysts.<sup>[82,83]</sup> Owing to their relative electrochemical inertness, they should be further investigated as catalytic supports for enhancing extrinsic catalytic activity. These benefits are clear when comparing the Cu–Pd/MXene with the Cu-based (Table S3, Supporting Information) and Sn-based (Table S4, Supporting Information) electrocatalysts reported for the electroreduction of CO<sub>2</sub> to formate. Cu–Pd/MXene catalyst clearly shows a remarkable activity and selectivity toward the electroreduction of CO<sub>2</sub> to formate with the lowest potential compared to all the reported literature for the production of formate.

### 4. Conclusion

In conclusion, we have synthesized and compared 3D-Cu–Pd and 3D bimetallic Cu–Pd/MXene aerogels for the electroreduction of CO<sub>2</sub>, which have been shown to efficiently convert CO<sub>2</sub> to C1 products. The H-cell study showed Cu–Pd/MXene suppressed HER and promoted the conversion of CO<sub>2</sub> to formate at a lower potential of –0.5 V versus RHE compared to Cu–Pd aerogel (–0.8 V vs RHE). Using a zero gap MEA cell, we

found that Cu–Pd/MXene catalyst exhibits a higher selectivity for formate production over CO and H<sub>2</sub> with the FE<sub>formate</sub>: 93% and *j*<sub>formate</sub>: 150 mA cm<sup>-2</sup> compared to Cu–Pd with the FE<sub>CO</sub>: 91% and *j*<sub>CO</sub>: 50 mA cm<sup>-2</sup>. The success of this catalyst design is attributed to 1) the synergy between Cu and Pd, which modifies the electronic structure and product selectivity; 2) the 3D-porous aerogel structure that increases catalytic surface area and CO<sub>2</sub> transport pathways; and 3) the unique multilayer composition of MXene enabling high conductivity. Our results provide new design concepts for boosting the performance of formate-producing catalysts by regulating surface and electronic structure to increase the electrochemically-accessible surface area toward efficient CO<sub>2</sub>-to-formate electroreduction.

## 5. Experimental Section

**Reagents and Chemicals:** All reagents and solvents were of commercial reagent grade and were used without further purification except where noted. K<sub>2</sub>CO<sub>3</sub> (99.99%), H<sub>2</sub>PdCl<sub>4</sub> (99%), CuCl<sub>2</sub> (99%), Ti<sub>3</sub>AlC<sub>2</sub> (90%), NH<sub>4</sub>HF<sub>2</sub> (99.99%), NaBH<sub>4</sub> (99%), D<sub>2</sub>O (>99.8%), were purchased from Sigma Aldrich. In the case of H-cell, Nafion- N-115 perfluorinated ion-exchange membrane with a thickness of 127 microns was used and purchased from Ion Power Company. For the MEA cell, Sustainion X37-50 Grade RT membrane was used and purchased from Dioxide Materials (US). All the experimental solutions were prepared using deionized water purified by a Millipore Milli-Q water purification system (18.2 MΩ cm). The glassy carbon surface was polished with 1, 0.3, and 0.05 μm alumina slurries in sequence for 10 min each. The electrodes were then ultrasonicated in acetone, ethanol, and water. All GCE electrochemically activated before drop-casting of modifier by cyclic voltammetry using potential ranges -0.5–1.5 V (vs Ag/AgCl (3 M KCl)) in a 1 M H<sub>2</sub>SO<sub>4</sub> solution with scan rate of 100 mV s<sup>-1</sup> for 15 cycles.

**Material and Characterizations:** All the spectroscopy data for the structural characterizations were obtained using the research facilities at the Delft University of Technology and the University of Toronto. The liquid products were analyzed using high-performance liquid chromatography (HPLC, Agilent 1200 HPLC using an Agilent HiPlex-H column 300 × 7.7 mm with 20 mm H<sub>2</sub>SO<sub>4</sub> as mobile phase at 0.6 mL min<sup>-1</sup> rate), and proton nuclear magnetic resonance (<sup>1</sup>H NMR) using a Bruker-400 NMR spectrometer. The concentration of gaseous products was obtained from GC with an average of four injections to calculate their Faradaic efficiencies. The gas products from the CO<sub>2</sub> electroreduction were analyzed using chromatograph (InterScience PerkinElmer Clarus 680) coupled with two thermal conductivity detectors (TCD) and a flame ionization detector (FID).

**HPLC Sample Calculation:** The formate ions (HCOO<sup>-</sup>) present in the liquid analyte were detected from HPLC measurements, and the Faradaic efficiency was calculated using the following equation (equation (1)). Here, a sample calculation for the CO<sub>2</sub>RR performed for 20 min for the Cu–Pd/MXene catalyst at 25 mA cm<sup>-2</sup> is shown. The volume of analyte used in the experiment was 200 mL (0.5 M KOH).

$$[\text{HCOO}^-] \text{ detected in analyte} = 1.2193 \text{ gL}^{-1} \quad (1)$$

$$\text{Molecular weight of HCOO}^- = 45 \text{ g mol}^{-1} \quad (2)$$

$$\text{Volume of analyte used} = 0.2 \text{ L} \quad (3)$$

$$\text{Moles of HCOO}^- = \frac{1.2193 \text{ gL}^{-1}}{45 \text{ g mol}^{-1}} \times 0.2 \text{ L} = 0.005419 \text{ moles} \quad (4)$$

$$\text{FE}_{\text{HCOO}^-} = \frac{\text{Moles of HCOO}^- \times n \times F}{I \times t} \times 100\% = \frac{0.005419 \times 2 \times 96485}{0.9375 \text{ A} \times 1200 \text{ s}} = 92.9\% \quad (5)$$

**<sup>1</sup>H NMR Analysis:** The NMR experiments were conducted with a Bruker-400 NMR spectrometer and were processed in MestreNova. A water suppression technique was applied to make the products' peaks more visible. 400 μL analyte of the MEA cell was taken directly, and 50 μL DMSO (7 mm) was used as an internal standard along with 50 μL D<sub>2</sub>O as solvent.

The molar concentration (mM) of the reduced product (formate) was calculated using the <sup>1</sup>H NMR spectrum as below:

NMR sample contains:

$$V_{\text{NMR sample}} = 400 \mu\text{L analyte} + 50 \mu\text{L D}_2\text{O} + 50 \mu\text{L external standard (DMSO)} = 500 \mu\text{L} \quad (6)$$

All parameters, such as the number of scans (32) parameters were consistent for all the experiments. <sup>1</sup>H-NMR signals were integrated and normalized with respect to DMSO. The molar concentration of formate was calculated using the below equation (Equation (2)):

$$C_x = \frac{I_x}{I_{\text{std}}} \cdot \frac{N_{\text{std}}}{N_x} \cdot C_{\text{std}} \quad (7)$$

where in the current work, “C<sub>x</sub>” is the molar concentration of the product (formate), “I<sub>x</sub>” is integral of the product, “I<sub>std</sub>” is integral of the internal standard (DMSO), “N<sub>std</sub>” is the number of protons in DMSO, “N<sub>x</sub>” is a number of protons in the product, and “C<sub>std</sub>” is the total concentration of DMSO. “n” is the number of electrons for formate production from CO<sub>2</sub> (Table S5, Supporting Information).

Next, the FE of the only achieved liquid product (formate) was calculated as below (Equation (3); and Table S5, Supporting Information):

$$\text{FE}_x = \frac{C_x \cdot V_{\text{NMR tube}} \cdot V_{\text{catholyte}}}{V_{\text{NMR sample}}} \cdot n \cdot F \quad (8)$$

where in the current work, “C<sub>x</sub>” is the molar concentration of the product, “V<sub>NMR tube</sub>” is 500 μL (400 μL NMR sample + 50 μL D<sub>2</sub>O + 50 μL DMSO), “V<sub>electrolyte</sub>” is 400 mL, “V<sub>NMR sample</sub>” is 400 μL, “n” is the number of electrons to be exchanged to produce, and “F” is Faraday's constant (96485.3). The net current flux across the electrical circuit is in Amperes, shown with “I” and “t” is the total time in seconds.

$$\text{FE}_{\text{Formate}} = \frac{0.01085 \cdot \frac{500 \cdot 10^{-6} \cdot 400 \cdot 10^{-3}}{400 \cdot 10^{-6}} \cdot 2 \cdot 96485.3}{0.9375 \cdot 1200} \cdot 100\% = 93.1\% \quad (9)$$

The gas products observed in the cathodic compartment were periodically collected from the reaction headspace and tested by gas chromatography (GC). The gas outlet of the electrolysis cell (either H-cell or flow-cell assembly) was connected to the sampling port of the GC, which injects a certain volume of the pre-chamber filled with saturated product gas from CO<sub>2</sub> electrolysis. An injection loop takes ≈5 min including the back-flush and stabilization time. A Molsieve-S4 column connected to a thermal conductivity detector (TCD) was used to analyze hydrogen (H<sub>2</sub>) and carbon monoxide (CO) gases.

The gaseous products (here denoted as “i”) were quantified according to the formula (Equation (4)):

$$\text{FE}(i)\% = \frac{n_i \cdot F \cdot \phi_i \cdot v_{\text{MFM}}}{I \cdot t} \quad (10)$$

where “n<sub>i</sub>” is the number of the electrons needed for CO<sub>2</sub> reduction to product, “F” is the Faraday constant, “φ<sub>i</sub>” is the volume fraction of the gases, “v<sub>MFM</sub>” is the molar gas flow rate measured by mass flow meter at the cell outlet and corrected according to the product mixture, “I” is the current measured at the time of the injection, and “t” is the total time in seconds.

Surface characterizations were performed using a FEI Helios G4 CX Scanning Electron Microscopy (SEM) using secondary electron imaging with immersion lens mode and a 15 kV electron acceleration voltage, and a Quanta Feg 250 Field-Emission Scanning Electron Microscope. X-ray photoelectric spectroscopy (XPS) analyses were performed with a

Theta-probe Thermo-Fisher Scientific Instrument (East Grinstead, UK) with a monochromatic  $K\alpha$  source with a photo energy of 1486.6 eV. The accumulated angle was  $90^\circ$  with a 20 eV pass energy at the analyzer in an 8–10 mbar vacuum chamber. The spectra were processed using the system's software (A vantage v5.986). A modified Shirley background was used for the baseline. A 30% Lorentzian/Gaussian mix was used for symmetric peaks; however, this was allowed to vary for the asymmetric peaks (C 1s  $sp^2$  peak and the main Pd 3d spin-orbit pairs). The  $3d_{3/2}$  features were constrained to the  $3d_{5/2}$  features for both Cu and Pd using the appropriate spin-orbit parameters. This was also done for the Pd 3p spin-orbit pair as the O 1s peak overlaps with Pd  $3p_{3/2}$  peak. Thus, by collecting the Pd  $3p_{1/2}$  and applying the spin-orbit parameters, the Pd  $3p_{3/2}$  contribution to the O 1s peak intensity could be subtracted.

X-ray diffraction (XRD) using a Bruker D8 Advanced diffractometer with Cu- $K\alpha$  source (Cu radiation wavelength:  $K\alpha_1(100) = 1.54060 \text{ \AA}$ ,  $K\alpha_2(50) = 1.54439 \text{ \AA}$ ) and Lynxeye-XE-T position-sensitive detector. Geometry radius: 250.0 mm. Power: 40 kV and 25 mA. a step size of  $0.1^\circ$ , and a measuring time of 0.1 s/step were employed. Geometry: theta-theta geometry (often called Bragg-Brentano or focusing geometry). A motorized varied-divergent slit of 5 mm. The scan range of  $2\theta$  is from  $5-90^\circ$ . The data evaluation was conducted using Bruker software DiffraSuite. EVA versus 5.1. database Pd (PDF 01–1201). The lattice parameter for Cu–Pd was observed as  $a = b = c = 3.8824 \text{ \AA}$  with a crystallite size of  $\approx 145 \text{ \AA}$ , which was in good agreement with Pd from the database (PDF 01–1201). For Cu–Pd/MXene, the lattice parameter:  $a = b = c = 3.8568 \text{ \AA}$ , smaller than that of Pd from the database (PDF 01–1201) was achieved with the crystallite size of Cu–Pd:  $\approx 71 \text{ \AA}$ . The peak at  $2\theta = 7.291^\circ$ , comes from the 002 peak of  $Ti_3C_2$ -MXene the lattice parameter,  $c = 24.23 \text{ \AA}$ .

**Synthesis of  $Ti_3C_2Tx^{[84]}$ :** i) The 2D  $Ti_3C_2$  was prepared by etching off the Al layer from  $Ti_3AlC_2$ . 1 g of  $Ti_3AlC_2$  powder was added to 20 ml of 1 M  $NH_4HF_2$  in a Teflon container under continuous stirring. The mixture was sonicated in an ultrasonic bath for 30 min at room temperature allowing Al atoms to be etched off. The first XRD patterns were performed in Figure S14 (Supporting Information). ii) The mixture was transferred to a stainless-steel autoclave container and kept at  $120^\circ\text{C}$  for 4 h. Next, to remove any remaining reaction by-products, the dark green suspension was rinsed three times with 200 ml of 0.1 M HCl, ethanol and water, respectively and dried under a vacuum for 24 h.

**Synthesis of Cu–Pd Aerogels:** The bimetallic Cu–Pd hydrogels were prepared using a simple procedure.<sup>[32,85,86]</sup> First, an aqueous solution of glyoxylic acid (100 mg) and sodium carbonate (500 mg) was added into a 10 mL solution of  $H_2PdCl_4$  (5 mM) and 3.5 mg  $CuCl_2$  (2.5 mM) under stirring.<sup>[85]</sup> The mixture was sonicated for 10 min to achieve a bright yellow solution.<sup>[86]</sup> Next, the glassy vial containing the suspension was transferred into the oven and allowed to settle at  $70^\circ\text{C}$  for 1 h to obtain a dark gray color. After cooling down the solution to room temperature, 35 mg of  $NaBH_4$  was added to the solution to complete the reduction process. Next, the temperature was increased to  $40^\circ\text{C}$  for another 3 h to form the Cu–Pd hydrogel. The achieved Cu–Pd hydrogel was washed with distilled water, ethanol, and acetone (20 mL, 3 times each in sequences), followed by overnight freeze-drying using a lyophilizer to obtain porous Cu–Pd aerogels.

**Synthesis of Cu–Pd/MXene Aerogels:** In the case of Cu–Pd/MXene fabrication, the same steps as Cu–Pd synthesis were followed. But, 3 mg of the synthesized  $Ti_3C_2$  was added into the  $H_2PdCl_4$  and  $CuCl_2$  solution before adding the reducing agents. The Cu–Pd/MXene hydrogel was formed through hydrothermal treatment followed by lyophilization to form a black and highly porous Cu–Pd/MXene hybrid aerogel with a 3D structure. It should be noted that the gelation process is fast and works efficiently, hence protecting the MXene from oxidation.

**H-Cell Electrochemical Measurements:** The electrochemical studies were carried out under  $CO_2/Ar$  in a sealed two-compartment electrochemical H-cell setup including 1) glassy carbon electrode (0.3 cm diameter), with a geometrical electrode area of  $0.071 \text{ cm}^2$  which was modified with aerogel to be served as a working electrode; 2) Pt wire auxiliary electrode; 3) Ag/AgCl reference electrode. The 0.1 M  $KHCO_3$  was used as both anolyte and catholyte. The anode and cathode chambers were separated via a Nafion membrane. The Nafion membrane was placed in 3%  $H_2O_2$  in a beaker

and heated up for 1 h at  $80^\circ\text{C}$ . Then it was rinsed with Milli-Q water three times and was heated up again for another 2 h at  $80^\circ\text{C}$  followed by another 1 h in 0.5 M  $H_2SO_4$  at the same temperature ( $80^\circ\text{C}$ ). Next, the solution was cooled down, and the membrane was rinsed with Milli-Q water three times. The membrane was stored in 1M  $KHCO_3$ .

Prior to each experiment, the glassy carbon surface was polished with 1, 0.3, and 0.05  $\mu\text{m}$  alumina slurries, respectively, and ultrasonicated in acetonitrile, ethanol, and water. To prepare the electrode for H-cell, 5 mg of the ground aerogels was mixed with Nafion (2%), then 5  $\mu\text{L}$  of the mixture was drop cast onto a glassy carbon electrode and allowed to air dry. The CHI 660C potentiostat (CH Instruments, Austin, TX) connected to a GC was equipped with a packed Molecular Sieve 5A capillary column and a packed HaySep D column. Helium (99.999%) was used as the carrier gas. A helium ionization detector (HID) was used to quantify gas product ( $H_2$  and CO) concentrations.

Linear sweep voltammetry (LSV) measurements were conducted with a positive initial scan polarity, 5 s quiet, and a scan rate of  $0.1 \text{ V s}^{-1}$ . All potentials were converted from Ag/AgCl (3 M KCl) to RHE ( $E_{RHE} = E_{Ag/AgCl} + 0.0591 \times \text{pH} + 0.210$ ).

The reported Faradic efficiency (FE) and current density ( $j$ ) were average values based on four reactions run with GC measurements taken every 15 min for 2 h. All the calculation was based on the geometrical surface area.

**MEA Cell Electrochemical Measurements:** All experiments were performed in a  $5 \text{ cm}^2$  membrane electrode assembly (Dioxide materials) electrolyzer with a serpentine flow channel on the anode and cathode endplates which were separated by Sustainion membrane. Nickel foam ( $3 \text{ cm} \times 3 \text{ cm}$ ) was used as the anode. Sigracet 38 BC gas diffusion layer (GDL) of  $5 \text{ cm}^2$  area was used as the porous transport layer. The Cu–Pd (10 mg) and Cu–Pd/MXene (10 mg) catalysts were dispersed in 1 mL of Dimethylformamide (DMF) individually and sonicated for 15 min to achieve a homogeneous black ink. Next, the catalysts were painted onto GDL to be served as a cathode. The GDE was left in the vacuum oven at  $80^\circ\text{C}$  for 3 h. The painting and drying were repeated until the desired catalyst loading of  $0.5 \text{ mg cm}^{-2}$  was achieved.

The GDE and Ni foam (Recemat BV) was combined with an oversized  $16 \text{ cm}^2$  ( $4 \text{ cm} \times 4 \text{ cm}$ ) Sustainion anion exchange membrane (X37-50 Grade RT) to assemble the MEA. The Sustainion membrane was pre-treated in 1 M KOH for 24 h. After removing the liners after 24 h, the membranes were treated in fresh 1 M KOH solution for another 24 h before use. An exchange MEA configuration using KOH (0.5 M) as the anolyte was fed at  $20 \text{ mL min}^{-1}$  using a peristaltic pump and recirculated into the anolyte reservoir. This concentration was chosen to reduce the crossover of  $K^+$  ions to the cathode side, which delays subsequent accumulation and salt precipitation at the cathode. On the cathode side,  $CO_2$  was bubbled into a humidifier with a flow rate of 50 sccm.

At the cathode, humidified  $CO_2$  at a flow rate of 50 sccm was fed into the reactor. The humidified  $CO_2$  helps the membrane stay hydrated and increases  $CO_2$  reduction stability. In addition, since  $H_2O$  is a reactant for  $CO_2RR$ , supplying  $H_2O$  in the gas phase helps reduce the necessary flux of water getting transported from the anolyte in the form of hydrated  $K^+$  ions. Hence, humidifying helps reduce  $K^+$  crossover from the anolyte and delays salt precipitation at the cathode, as shown in a previous study.<sup>[87]</sup>

A series of constant current electrolysis experiments were performed, and the gaseous products from the outlet were analyzed using online gas chromatography (GC). The GC was equipped with two thermal conductivity detectors and a flame ionization detector to identify hydrocarbons, CO and  $H_2$  separately. Constant current electrolysis at different current densities starting from 25 to  $200 \text{ mA cm}^{-2}$ , was performed for 1200 s at each current density. Aliquots were collected every 5 min during the reaction resulting in a total of 4 injections for each current density in 1200 s. The flow rate at the reactor outlet was measured using a mass flow meter (Bronkhorst) to estimate the faradaic efficiency of products accurately. A LABVIEW program was built and connected to the mass flow meter to monitor the outlet flow rate continuously. The outlet flow rate of the gas mixture ( $CO + H_2 + \text{residual } CO_2$ ) from the reactor was measured ( $\dot{V}_{\text{outlet}}$ ) using the mass flow meter

and the mole fractions of CO ( $x_{CO}$ ) and H<sub>2</sub> ( $x_{H_2}$ ) were estimated from the GC injections.

**Electrochemically Active Surface Area (ECSA):** The double-layer capacitive current ( $C_{dl}$ ) was estimated by plotting the current density at 0.15 V versus Ag/AgCl against the scan rate (mV/s). The  $C_{dl}$  of an ideal smooth surface is 60  $\mu\text{F cm}^{-2}$ . The roughness factor ( $R_f$ ) of the electrodes was calculated using Equation (5):<sup>[88,89]</sup>

$$R_f = \frac{C_{dl}}{60} \quad (11)$$

From Equation (5) and the electrode surface area of 0.071  $\text{cm}^2$ , the ECSA was calculated using Equation (6):

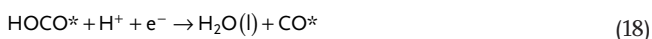
$$\text{ECSA} = R_f \times S_{\text{electrode}} \quad (12)$$

**Computational Details:** All the calculations reported in this article were performed by Vienna ab initio simulation package (VASP)<sup>[90]</sup> based on periodic plane-wave density functional theory (DFT). The interactions between ion cores and valence electrons were accounted by the projector-augmented wave (PAW)<sup>[91]</sup> pseudopotentials. The exchange and correlation interactions between electrons was treated within the generalized gradient approximation (GGA)<sup>[92]</sup> with the Perdew-Burke-Ernzerhof (PBE)<sup>[93]</sup> parameterization. The additional van der Waals (vdW) contributions were obtained through the DFT-D3 method.<sup>[94]</sup> The cut off energy for expanded plane-wave basis set was set to 500 eV. The convergence thresholds for full geometry optimizations were set to  $10^{-5}$  eV and 0.005 eV  $\text{\AA}^{-1}$  for each electronic and ionic steps, respectively. The vacuum space ( $d_{\text{vac}}$ ) at least 20  $\text{\AA}$  was set between repeat slab along the z directions to avoid periodic interactions. The  $25 \times 25 \times 25 \text{\AA}$  unit cell box was used for calculation of isolated molecule. The model of Cu–Pd system was constructed from the  $3 \times 3 \times 3$  Cu(111) slab surface with one Cu atom substituted by Pd. The slab consists of six atomic layers, of which the top four layers were allowed to relax. Whereas the structure of Cu–Pd/MXene was generated from the MXene surface with Pd adatom on top of the MXene surface.

The mechanism of the electrochemical conversion reaction of CO<sub>2</sub> to HCOOH\* is represented by the following equations.



and



Symbol \* represents the active site on the surface, and any molecule with \* indicates the adsorbed intermediate species on the surface. Moreover, the zero-point energy (ZPE) and entropy correction were also used to convert the DFT energies into Gibbs free energies of adsorption ( $\Delta G$ ) through the formula as follows:

$$\Delta G = \Delta E + \Delta \text{ZPE} - T\Delta S \quad (19)$$

Where,  $\Delta E$  is the total energy difference between the product and the reactant, the  $\Delta \text{ZPE}$  is the change in zero-point energy, the  $T$  is the temperature, and  $\Delta S$  is the change in entropy. The ZPE and  $S$  values were obtained from the literature.<sup>[95]</sup>

The computational standard hydrogen electrode (CHE) model was used to constructing the reaction pathway of the electrochemical conversion reaction of CO<sub>2</sub> to HCOOH and/or CO on Cu–Pd and Cu–Pd/MXene. In CHE model, the chemical potential of a proton/electron ( $\text{H}^+ + \text{e}^-$ ) can be reference with a half of the chemical potential

of a gaseous H<sub>2</sub>. The free energies change ( $\Delta G$ ) for each reaction step is given by the following equation:

$$\Delta G = \Delta E + \Delta \text{ZPE} - T\Delta S + \Delta G_{\text{U}} + \Delta G_{\text{pH}} + \Delta G_{\text{field}} \quad (20)$$

In this calculation, the standard condition, pH = 0 and  $T = 298.15 \text{ K}$  and  $U = 0$  are set.

The adsorption energies were calculated as the difference between total energy of a system, the energy of the substrate, and CO<sub>2</sub> molecule energy (Equation (9)).

$$E_{\text{ads}} = E_{\text{tot}} - E_{\text{sub}} - E_{\text{mol}} \quad (21)$$

The CO<sub>2</sub> adsorption on Cu–Pd is stronger than on Cu–Pd/Mxene with adsorption energies  $-0.189 \text{ eV}$  for Cu–Pd substrate and  $-0.109 \text{ eV}$  for Cu–Pd/Mxene.

**Thermogravimetric Analysis (TGA) of CO<sub>2</sub> Adsorption Capacity:** In order to study the thermal decomposition of the samples, Thermogravimetric analysis (TGA) TGA was carried out in a mixture of N<sub>2</sub> and air from 25 to 750 °C at a heating rate of 10 °C min<sup>-1</sup> on a METTLER TOLEDO SF/1100 thermogravimetric analyzer. For the estimation of the CO<sub>2</sub> adsorption capacity,  $\approx 5 \text{ mg}$  of each sample was heated from 25 to 105 °C at 20 °C min<sup>-1</sup> under N<sub>2</sub>.<sup>[63,96]</sup> The samples were held at 105 °C for 30 min and then cooled to the desired temperature at 10 °C min<sup>-1</sup>. The gas input was switched from N<sub>2</sub> to CO<sub>2</sub> and held isothermally for 90 min. The CO<sub>2</sub> adsorption capacity was determined from the weight change observed in the CO<sub>2</sub> pulse. Effects of the change in gas viscosity and gas density were corrected by measuring the response to an empty platinum crucible by the same method.

## Supporting Information

Supporting Information is available from the Wiley Online Library or from the author.

## Acknowledgements

The authors would also like to thank Xiaohui Liu and Bart Boshuizen for their help and support on the XPS and XRD studies. H.B.K. would like to acknowledge the Natural Sciences and Engineering Research Council of Canada (NSERC DG-2022-03129), and the University of Toronto. S.D. would like to acknowledge support from Acceleration Consortium (AC) for postdoctoral fellowships. I.N. would like to acknowledge the University of Toronto for the Connaught International Scholarship. O.V. would like to acknowledge the Natural Sciences and Engineering Research Council of Canada (NSERC Discovery 2019-04807). This research was enabled in part by support provided by SciNet and Compute Canada.

## Conflict of Interest

The authors declare no conflict of interest.

## Author Contributions

M.A., S.S., and M.K.M. contributed equally to this work. M.A. and T.B. wrote the original draft of the manuscript and all authors reviewed the manuscript.

## Data Availability Statement

The data that support the findings of this study are available from the corresponding author upon reasonable request.



## Keywords

CO<sub>2</sub> Electrolysis, Copper-based electrocatalysts, formate, Membrane-electrode assemblies, MXene

Received: February 7, 2023

Revised: March 13, 2023

Published online:

- [1] T. R. Knutson, R. E. Tuleya, *J. Clim.* **2004**, *17*, 3477.
- [2] J. Wu, T. Sharifi, Y. Gao, T. Zhang, P. M. Ajayan, *Adv. Mater.* **2019**, *31*, 1804257.
- [3] M. Li, K. Yang, M. Abdinejad, C. Zhao, T. Burdyny, *Nanoscale* **2022**, *14*, 11892.
- [4] D. Higgins, C. Hahn, C. Xiang, T. F. Jaramillo, A. Z. Weber, *ACS Energy Lett.* **2019**, *4*, 317.
- [5] P. De Luna, C. Hahn, D. Higgins, S. A. Jaffer, T. F. Jaramillo, E. H. Sargent, *Science* **2019**, *364*, eaav3506.
- [6] C. G. Morales-Guio, E. R. Cave, S. A. Nitopi, J. T. Feaster, L. Wang, K. P. Kuhl, A. Jackson, N. C. Johnson, D. N. Abram, T. Hatsukade, C. Hahn, T. F. Jaramillo, *Nat. Catal.* **2018**, *1*, 764.
- [7] M. Abdinejad, E. Irtam, A. Farzi, M. Sassenburg, S. Subramanian, H.-P. I. van Montfort, D. Ripepi, M. Li, J. Middelkoop, A. Seifitokaldani, T. Burdyny, *ACS Catal.* **2022**, *12*, 7862.
- [8] M. Abdinejad, I. Santos da Silva, H. B. Kraatz, *J. Mater. Chem. A* **2021**, *9*, 9791.
- [9] M. Abdinejad, M. K. Motlagh, M. Noroozifar, H. B. Kraatz, *Mater. Adv.* **2022**, *3*, 1224.
- [10] M. Abdinejad, T. Yuan, K. Tang, S. Duangdangchote, A. Farzi, H.-P. I. van Montfort, M. Li, J. Middelkoop, M. Wolff, A. Seifitokaldani, O. Voznyy, T. Burdyny, *Chem. – Eur. J.* **2022**, *29*, 202203977.
- [11] X. Lu, Y. Wu, X. Yuan, H. Wang, *Angew. Chem., Int. Ed.* **2019**, *58*, 4031.
- [12] E. Kjeang, R. Michel, D. A. Harrington, D. Sinton, N. Djilali, *Electrochim. Acta* **2008**, *54*, 698.
- [13] S. Zhang, P. Kang, T. J. Meyer, *J. Am. Chem. Soc.* **2014**, *136*, 1734.
- [14] X. Zheng, Y. Ji, J. Tang, J. Wang, B. Liu, H.-G. Steinrück, K. Lim, Y. Li, M. F. Toney, K. Chan, Y. Cui, *Nat. Catal.* **2019**, *2*, 55.
- [15] X. Zheng, P. De Luna, F. P. G. de Arquer, B. Zhang, N. Becknell, M. B. Ross, Y. Li, M. N. Banis, Y. Li, M. Liu, O. Voznyy, C. T. Dinh, T. Zhuang, P. Stadler, Y. Cui, X. Du, P. Yang, E. H. Sargent, *Joule* **2017**, *1*, 794.
- [16] S. Zhao, S. Li, T. Guo, S. Zhang, J. Wang, Y. Wu, Y. Chen, *Nano-Micro Lett.* **2019**, *11*, 62.
- [17] Z. B. Hoffman, T. S. Gray, K. B. Moraveck, T. B. Gunnoe, G. Zangari, *ACS Catal.* **2017**, *7*, 5381.
- [18] Z. M. Detweiler, J. L. White, S. L. Bernasek, A. B. Bocarsly, *Langmuir* **2014**, *30*, 7593.
- [19] C. H. Lee, M. W. Kanan, *ACS Catal.* **2015**, *5*, 465.
- [20] J. E. Pander, J. W. J. Lum, B. S. Yeo, *J. Mater. Chem. A* **2019**, *7*, 4093.
- [21] B. Ren, G. Wen, R. Gao, D. Luo, Z. Zhang, W. Qiu, Q. Ma, X. Wang, Y. Cui, L. Ricardez-Sandoval, A. Yu, Z. Chen, *Nat. Commun.* **2022**, *13*, 2486.
- [22] C. T. Dinh, T. Burdyny, G. Kibria, A. Seifitokaldani, C. M. Gabardo, F. P. G. De Arquer, A. Kiani, J. P. Edwards, P. De Luna, O. S. Bushuyev, C. Zou, R. Quintero-Bermudez, Y. Pang, D. Sinton, E. H. Sargent, *Science* **2018**, *360*, 783.
- [23] M. Abdinejad, Z. Mirza, X. A. Zhang, H. B. Kraatz, *ACS Sustainable Chem. Eng.* **2020**, *8*, 1715.
- [24] J. Greeley, T. F. Jaramillo, J. Bonde, I. Chorkendorff, J. K. Nørskov, *Nat. Mater.* **2006**, *5*, 909.
- [25] Q. Li, Y. Zhang, X. Zhang, H. Wang, Q. Li, J. Sheng, J. Yi, Y. Liu, J. Zhang, *Ind. Eng. Chem. Res.* **2020**, *59*, 6806.
- [26] Y. Mun, S. Lee, A. Cho, S. Kim, J. W. Han, J. Lee, *Appl. Catal. B* **2019**, *246*, 82.
- [27] Z. Yin, D. Gao, S. Yao, B. Zhao, F. Cai, L. Lin, P. Tang, P. Zhai, G. Wang, D. Ma, X. Bao, *Nano Energy* **2016**, *27*, 35.
- [28] T. Takashima, T. Suzuki, H. Irie, *Electrochemistry* **2019**, *87*, 134.
- [29] X. Jiang, X. Wang, Z. Liu, Q. Wang, X. Xiao, H. Pan, M. Li, J. Wang, Y. Shao, Z. Peng, Y. Shen, M. Wang, *Appl. Catal. B* **2019**, *259*, 118040.
- [30] A. Vasileff, C. Xu, Y. Jiao, Y. Zheng, S.-Z. Qiao, *Chem* **2018**, *4*, 1809.
- [31] J. Li, Y. Kuang, Y. Meng, X. Tian, W.-H. Hung, X. Zhang, A. Li, M. Xu, W. Zhou, C.-S. Ku, C.-Y. Chiang, G. Zhu, J. Guo, X. Sun, H. Dai, *J. Am. Chem. Soc.* **2020**, *142*, 7276.
- [32] M. Abdinejad, C. Ferrag, M. N. Hossain, M. Noroozifar, K. Kerman, H. B. Kraatz, *J. Mater. Chem. A* **2021**, *9*, 12870.
- [33] M. Naguib, M. Kurtoglu, V. Presser, J. Lu, J. Niu, M. Heon, L. Hultman, Y. Gogotsi, M. W. Barsoum, *Adv. Mater.* **2011**, *23*, 4248.
- [34] Q. Jiang, C. Wu, Z. Wang, A. C. Wang, J.-H. He, Z. L. Wang, H. N. Alshareef, *Nano Energy* **2018**, *45*, 266.
- [35] M. Naguib, V. N. Mochalin, M. W. Barsoum, Y. Gogotsi, *Adv. Mater.* **2014**, *26*, 992.
- [36] B. Anasori, M. R. Lukatskaya, Y. Gogotsi, *Nat. Rev. Mater.* **2017**, *2*, 16098.
- [37] J. Lipton, G.-M. Weng, M. Alhabeb, K. Maleski, F. Antonio, J. Kong, Y. Gogotsi, A. D. Taylor, *Nanoscale* **2019**, *11*, 20295.
- [38] U. Yorulmaz, A. Özden, N. K. Perkgöz, F. Ay, C. Sevik, *Nanotechnology* **2016**, *27*, 335702.
- [39] D. Xiong, X. Li, Z. Bai, S. Lu, *Small* **2018**, *14*, 1703419.
- [40] X. Xie, M.-Q. Zhao, B. Anasori, K. Maleski, C. E. Ren, J. Li, B. W. Byles, E. Pomerantseva, G. Wang, Y. Gogotsi, *Nano Energy* **2016**, *26*, 513.
- [41] Q. Zhao, C. Zhang, R. Hu, Z. Du, J. Gu, Y. Cui, X. Chen, W. Xu, Z. Cheng, S. Li, B. Li, Y. Liu, W. Chen, C. Liu, J. Shang, L. Song, S. Yang, *ACS Nano* **2021**, *15*, 4927.
- [42] A. VahidMohammadi, M. Mojtavavi, N. M. Caffrey, M. Wanunu, M. Beidaghi, *Adv. Mater.* **2019**, *31*, 1806931.
- [43] J. Liu, H.-B. Zhang, X. Xie, R. Yang, Z. Liu, Y. Liu, Z.-Z. Yu, *Small* **2018**, *14*, 1802479.
- [44] Y. Chen, C. Liu, S. Guo, T. Mu, L. Wei, Y. Lu, *Green Energy Environ.* **2022**, *7*, 394.
- [45] X. Wang, Q. Fu, J. Wen, X. Ma, C. Zhu, X. Zhang, D. Qi, *Nanoscale* **2018**, *10*, 20828.
- [46] S. Shi, B. Qian, X. Wu, H. Sun, H. Wang, H.-B. Zhang, Z.-Z. Yu, T. P. Russell, *Angew. Chem., Int. Ed.* **2019**, *58*, 18171.
- [47] M. R. Lukatskaya, O. Mashtalir, C. E. Ren, Y. Dall'Agnese, R. Patrick, T. P. Louis, M. Naguib, S. Patrice, M. W. Barsoum, Y. Gogotsi, *Science* **2013**, *341*, 1502.
- [48] N. Wu, B. Zhao, X. Chen, C. Hou, M. Huang, A. Alhadhrami, G. A. M. Mersal, M. M. Ibrahim, J. Tian, *Adv. Compos. Hybrid Mater.* **2022**, *5*, 1548.
- [49] K. Allen-Perry, W. Straka, D. Keith, S. Han, L. Reynolds, B. Gautam, D. E. Autrey, *Materials* **2021**, *14*, 694.
- [50] D. Chen, L. Xu, H. Liu, J. Yang, *Green Energy Environ.* **2019**, *4*, 254.
- [51] S. Ma, M. Sadakiyo, M. Heima, R. Luo, R. T. Haasch, J. I. Gold, M. Yamauchi, P. J. A. Kenis, *J. Am. Chem. Soc.* **2017**, *139*, 47.
- [52] L. Xiong, Y.-X. Huang, X.-W. Liu, G.-P. Sheng, W.-W. Li, H.-Q. Yu, *Electrochim. Acta* **2013**, *89*, 24.
- [53] C. J. Corcoran, H. Tavassol, M. A. Rigsby, P. S. Bagus, A. Wieckowski, *J. Power Sources* **2010**, *195*, 7856.
- [54] V. S. Sundaram, M. B. de Moraes, J. D. Rogers, G. G. Kleiman, *J. Phys. F: Met. Phys.* **1981**, *11*, 1151.
- [55] L. Li, X. Chen, Y. Wu, D. Wang, Q. Peng, G. Zhou, Y. Li, *Angew. Chem., Int. Ed.* **2013**, *52*, 11049.
- [56] D. A. Svintitskiy, T. Y. Kardash, O. A. Stonkus, E. M. Slavinskaya, A. I. Stadnichenko, S. V. Koscheev, A. P. Chupakhin, A. I. Boronin, *J. Phys. Chem. C* **2013**, *117*, 14588.



- [57] R. Kas, K. Yang, D. Bohra, R. Kortlever, T. Burdyny, W. A. Smith, *Chem. Sci.* **2020**, *11*, 1738.
- [58] S. Subramanian, J. Middelkoop, T. Burdyny, *Sustainable Energy Fuels* **2021**, *5*, 6040.
- [59] K. Liu, W. A. Smith, T. Burdyny, *ACS Energy Lett.* **2019**, *4*, 639.
- [60] L. Zabaleta, K. Gourrat, L. J. R. Barron, M. Albisu, E. Guichard, *Int. Dairy J.* **2016**, *58*, 23.
- [61] M. J. Al-Marri, Y. O. Kuti, M. Khraisheh, A. Kumar, M. M. Khader, *Chem. Eng. Technol.* **2017**, *40*, 1802.
- [62] Y. He, Y. Xia, J. Zhao, Y. Song, L. Yi, L. Zhao, *Appl. Phys. A* **2019**, *125*, 160.
- [63] J. Wang, L. A. Stevens, T. C. Drage, J. Wood, *Chem. Eng. Sci.* **2012**, *68*, 424.
- [64] R. V. Siriwardane, M.-S. Shen, E. P. Fisher, J. Losch, *Energy Fuels* **2005**, *19*, 1153.
- [65] X. Rong, H.-J. Wang, X.-L. Lu, R. Si, T.-B. Lu, *Angew. Chem., Int. Ed.* **2020**, *59*, 1961.
- [66] X. Sun, Y. Tuo, C. Ye, C. Chen, Q. Lu, G. Li, P. Jiang, S. Chen, P. Zhu, M. Ma, J. Zhang, J. H. Bitter, D. Wang, Y. Li, *Angew. Chem., Int. Ed.* **2021**, *60*, 23614.
- [67] T. Gao, X. Wen, T. Xie, N. Han, K. Sun, L. Han, H. Wang, Y. Zhang, Y. Kuang, X. Sun, *Electrochim. Acta* **2019**, *305*, 388.
- [68] Y. Chen, M. W. Kanan, *J. Am. Chem. Soc.* **2012**, *134*, 1986.
- [69] G. Jun, H. Chia-Shuo, B. Lichen, C. H. Ming, H. Xile, *Science* **2019**, *364*, 1091.
- [70] K. Ngamchuea, S. Eloul, K. Tschulik, R. G. Compton, *J. Solid State Electrochem.* **2014**, *18*, 3251.
- [71] X. Hou, Y. Cai, D. Zhang, L. Li, X. Zhang, Z. Zhu, L. Peng, Y. Liu, J. Qiao, *J. Mater. Chem. A* **2019**, *7*, 3197.
- [72] D. Li, J. Wu, T. Liu, J. Liu, Z. Yan, L. Zhen, Y. Feng, *Chem. Eng. J.* **2019**, *375*, 122024.
- [73] S. Subramanian, K. Yang, M. Li, M. Sassenburg, M. Abdinejad, E. Irttem, J. Middelkoop, T. Burdyny, *ACS Energy Lett.* **2022**, *8*, 222.
- [74] Y. Xu, J. P. Edwards, S. Liu, R. K. Miao, J. E. Huang, C. M. Gabardo, C. P. O'Brien, J. Li, E. H. Sargent, D. Sinton, *ACS Energy Lett.* **2021**, *6*, 809.
- [75] B. Endrődi, A. Samu, E. Kecsenovity, T. Halmágyi, D. Sebők, C. Janáky, *Nat. Energy* **2021**, *6*, 439.
- [76] M. Sassenburg, M. Kelly, S. Subramanian, W. A. Smith, T. Burdyny, *ACS Energy Lett.* **2023**, *8*, 321.
- [77] L. Li, A. Ozden, S. Guo, F. P. Garcia de Arquer, C. Wang, M. Zhang, J. Zhang, H. Jiang, W. Wang, H. Dong, D. Sinton, E. H. Sargent, M. Zhong, *Nat. Commun.* **2021**, *12*, 5223.
- [78] C. Xia, P. Zhu, Q. Jiang, Y. Pan, W. Liang, E. Stavitski, H. N. Alshareef, H. Wang, *Nat. Energy* **2019**, *4*, 776.
- [79] T.-D. Nguyen-Phan, L. Hu, B. H. Howard, W. Xu, E. Stavitski, D. Leshchev, A. Rothenberger, K. C. Neyerlin, D. R. Kauffman, *Sci. Rep.* **2022**, *12*, 8420.
- [80] D. Kim, J. Resasco, Y. Yu, A. M. Asiri, P. Yang, *Nat. Commun.* **2014**, *5*, 4948.
- [81] A. R. T. Morrison, M. Ramdin, L. J. P. van der Broeke, W. de Jong, T. J. H. Vlucht, R. Kortlever, *J. Phys. Chem. C* **2022**, *126*, 11927.
- [82] N. Li, X. Chen, W.-J. Ong, D. R. MacFarlane, X. Zhao, A. K. Cheetham, C. Sun, *ACS Nano* **2017**, *11*, 10825.
- [83] K. Mou, Z. Chen, X. Zhang, M. Jiao, X. Zhang, X. Ge, W. Zhang, L. Liu, *Small* **2019**, *15*, 1903668.
- [84] M. Alhabeb, K. Maleski, B. Anasori, P. Lelyukh, L. Clark, S. Sin, Y. Gogotsi, *Chem. Mater.* **2017**, *29*, 7633.
- [85] A. Shafaei Douk, H. Saravani, M. Noroozifar, *Electrochim. Acta* **2018**, *275*, 182.
- [86] A. S. Douk, H. Saravani, M. Z. Yazdan Abad, M. Noroozifar, *Composites, Part B* **2019**, *172*, 309.
- [87] D. G. Wheeler, B. A. W. Mowbray, A. Reyes, F. Habibzadeh, J. He, C. P. Berlinguette, *Energy Environ. Sci.* **2020**, *13*, 5126.
- [88] W. Deng, L. Zhang, L. Li, S. Chen, C. Hu, Z.-J. Zhao, T. Wang, J. Gong, *J. Am. Chem. Soc.* **2019**, *141*, 2911.
- [89] S. Levine, A. L. Smith, *Discuss. Faraday Soc.* **1971**, *52*, 290.
- [90] G. Kresse, J. Furthmüller, *Comput. Mater. Sci.* **1996**, *6*, 15.
- [91] G. Kresse, D. Joubert, *Phys. Rev. B* **1999**, *59*, 1758.
- [92] J. P. Perdew, K. Burke, M. Ernzerhof, *Phys. Rev. Lett.* **1996**, *77*, 3865.
- [93] J. P. Perdew, M. Ernzerhof, K. Burke, *J. Chem. Phys.* **1996**, *105*, 9982.
- [94] S. Grimme, J. Antony, S. Ehrlich, H. Krieg, *J. Chem. Phys.* **2010**, *132*, 154104.
- [95] J.-F. Xie, J.-J. Chen, Y.-X. Huang, X. Zhang, W.-K. Wang, G.-X. Huang, H.-Q. Yu, *Appl. Catal. B* **2020**, *270*, 118864.
- [96] P. J. E. Harlick, A. Sayari, *Ind. Eng. Chem. Res.* **2006**, *45*, 3248.